

Cluster-based multidimensional scaling embedding tool for data visualization

Patricia Hernández-León

PATRICIA.HERNANDEZLEON@AALTO.FI

*Department of Electrical Engineering and Automation
Aalto University
02150, Espoo, Finland*

Miguel A. Caro

MCAROBAGMAIL.COM

*Department of Electrical Engineering and Automation
Aalto University
02150, Espoo, Finland*

Abstract

We present a new technique for visualizing high-dimensional data called cluster MDS (cl-MDS), which addresses a common difficulty of dimensionality reduction methods: preserving both local and global structures of the original sample in a single 2-dimensional visualization. Its algorithm combines the well-known multidimensional scaling (MDS) tool with the k -medoids data clustering technique, and enables hierarchical embedding, sparsification and estimation of 2-dimensional coordinates for additional points. While cl-MDS is a generally applicable tool, we also include specific recipes for atomic structure applications. We apply this method to non-linear data of increasing complexity where different layers of locality are relevant, showing a clear improvement in their retrieval and visualization quality.

Keywords: dimensionality reduction, data visualization, cluster MDS, embedding algorithms, Machine Learning

1. Introduction

Data complexity is a reflection of the world’s complexity. This manifests itself in the presence of high-dimensional datasets in all fields of science and the humanities. Even though there are several types of data complexity, dimensionality alone can *per se* drastically reduce the insight (even the scientific knowledge) that we can extract from a given sample. In this context, data visualization can be very valuable, albeit extremely difficult to achieve with a high number of dimensions n (where high means $n > 3$). An obvious approach to tackle this problem is reducing the number of dimensions involved, so as to unravel the original information within our limited “visual/dimensional grasp”. In practice, this is essentially equivalent to finding a (satisfactory) map between a low-dimensional representation of the data (preferably within a 2–3 dimensional Euclidean space) and the original high-dimensional representation.

The so-called *dimensionality reduction techniques* are an example of how to achieve one such map, increasingly used thanks to the popularization of machine learning (ML) and data mining in most fields of science. These methods generate an (either linear or non-linear) embedding that leads to an optimized candidate low-dimensional representation of the original sample. Note that we refer to *candidate* representations; despite its existence,

the map is not necessarily unique nor exact (Lui et al., 2018). There is an unavoidable tradeoff between the amount of information preserved and the dimensionality reduction required, leading to a plethora of possible approaches and an extensive literature on the matter. Some of the best established among these techniques are principal component analysis (PCA) (Hotelling, 1933), t-distributed stochastic neighbor embedding (t-SNE) (van der Maaten and Hinton, 2008; van der Maaten, 2014), Isomap (Tenenbaum et al., 2000) and multidimensional scaling (MDS) (Kruskal, 1964a,b; Borg and Groenen, 2005). Such variety of methods is, however, a symptom of a deeper problem: while they aim for the same mathematical object, their outputs differ widely. More importantly, the differing representations/visualizations can lead to disagreement in the interpretation and retained knowledge that can be obtained from a dataset.

Ideally, a suitable goodness-of-fit test would allow the user to choose the best algorithm for a given sample. Unfortunately, there is no universal metric that measures the accuracy of the resulting embedding nor its quality as a visualization of the original sample (Lui et al., 2018; Bertini et al., 2011; Tsai, 2012), not to mention both simultaneously. Having no absolute measure of the quality of a method, a sensible approach is to reexamine the aforementioned techniques in order to overcome some of their particular shortcomings, usually with the objective to either obtain an overall mathematical improvement or a concrete domain-specific one. Examples of the former, such as the uniform manifold approximation and projection (UMAP) method (McInnes et al., 2020), focus on increasing the robustness of previous theoretical foundations, with special emphasis on their mathematically based algorithmic decisions. On the other hand, improvements for domain-specific applications are motivated by the poor performance and visualizations obtained for high-dimensional non-linear data, e.g., biological data in the case of the potential of heat diffusion for affinity-based transition embedding (PHATE) tool (Moon et al., 2019).

This paper introduces a new member of the last category that we call cluster MDS (cl-MDS) (Caro and Hernández-León, accessed September 14, 2022a), motivated by our work with atomic structures. This method arises from the need for an embedding tool which hierarchically preserves global and local features in the same visualization, given their significance when analyzing atomic databases. Due to the inherent local or global nature of the algorithms, just retaining local structures without detriment to global ones poses a serious challenge to the majority of dimensionality reduction techniques, especially to those favoring local distances over other scales (e.g., t-SNE and UMAP). In this context, methods that focus on preserving the global distance structure (e.g., MDS and Isomap) tend to perform better, but are heavily reliant on the distribution of local features of the dataset. cl-MDS is our attempt at combining the strengths of (metric) MDS with a data clustering technique, using a carefully devised algorithm that allows us to retrieve several layers of locality and to embed them consistently. Despite our background and motivation, we have developed this algorithm bearing a general approach in mind; while the nuances of each sample may differ across domains, they are likely to possess global and local structures that could benefit from this new tool.

This paper is organized as follows. Section 2 presents a detailed description of the cl-MDS algorithm and its general features. Domain-specific recipes for atomic structure visualization are given in Section 3. We show a diverse selection of examples in Section 4,

as well as some comparisons with other methods. The advantages and disadvantages of cl-MDS are discussed there too. We summarize and conclude in Section 5.

2. Cluster MDS algorithm

The main purpose of cl-MDS is to obtain a low-dimensional representation of some high-dimensional data, where the distances between data points resemble the original ones as much as possible, similarly to metric MDS (Borg and Groenen, 2005). However, the key additional constraint relates to preserving the maximum amount of local information while improving the visualization of global structures with a sole embedding. As discussed earlier, most of the current dimensionality reduction methods typically fail to capture that interplay between the local and global details, since they usually focus on either the former or the latter.

With this in mind, let us consider a sample of N data points $X = \{x_1, \dots, x_N\}$ contained in a high-dimensional metric space \mathbb{R}^n , where $n > 2$ and $\mathcal{I} = \{1, \dots, N\}$ denotes its set of indices. Given an associated distance matrix \mathbf{D} with elements D_{ij} for each $i, j \in \mathcal{I}$, the intended output of the algorithm is a low-dimensional representation $Y = \{y_1, \dots, y_N\}$ of X within \mathbb{R}^2 . Unlike other methods, the target number of dimensions m is fixed ($m = 2$) because cl-MDS has been developed as a visualization tool, rather than a general dimensionality reduction technique. Also, note that the notion of distance refers here to any metric function defined on X , which will be used as a dissimilarity measure.

The algorithm consists of three parts. The first and second are responsible for identifying the local and global structure of X , respectively, and computing their corresponding (independent) 2-dimensional embeddings. Since those mappings give rise to different representations in \mathbb{R}^2 , the third part of the algorithm seeks to reconcile the information (local and global) into a single representation, leading to $Y \subset \mathbb{R}^2$. More specifically, the following steps are performed (see Fig. 1):

A. Identify local structures

1. Clustering using k -medoids, with $k = N_{\text{cl}}$, separates the dataset into N_{cl} data clusters.
2. MDS embedding of each cluster, separately (N_{cl} independent local maps).

B. Identify the global structure

3. Selection of reference (*anchor*) points in each cluster.
4. Joint MDS embedding of reference points only (global map).

C. From local to global embedding

5. Checking for pathological configurations.
6. Carry local representation over to the global map, preserving the local structure of the data.

These steps constitute the core of the cl-MDS algorithm and are further explained in the following subsections.

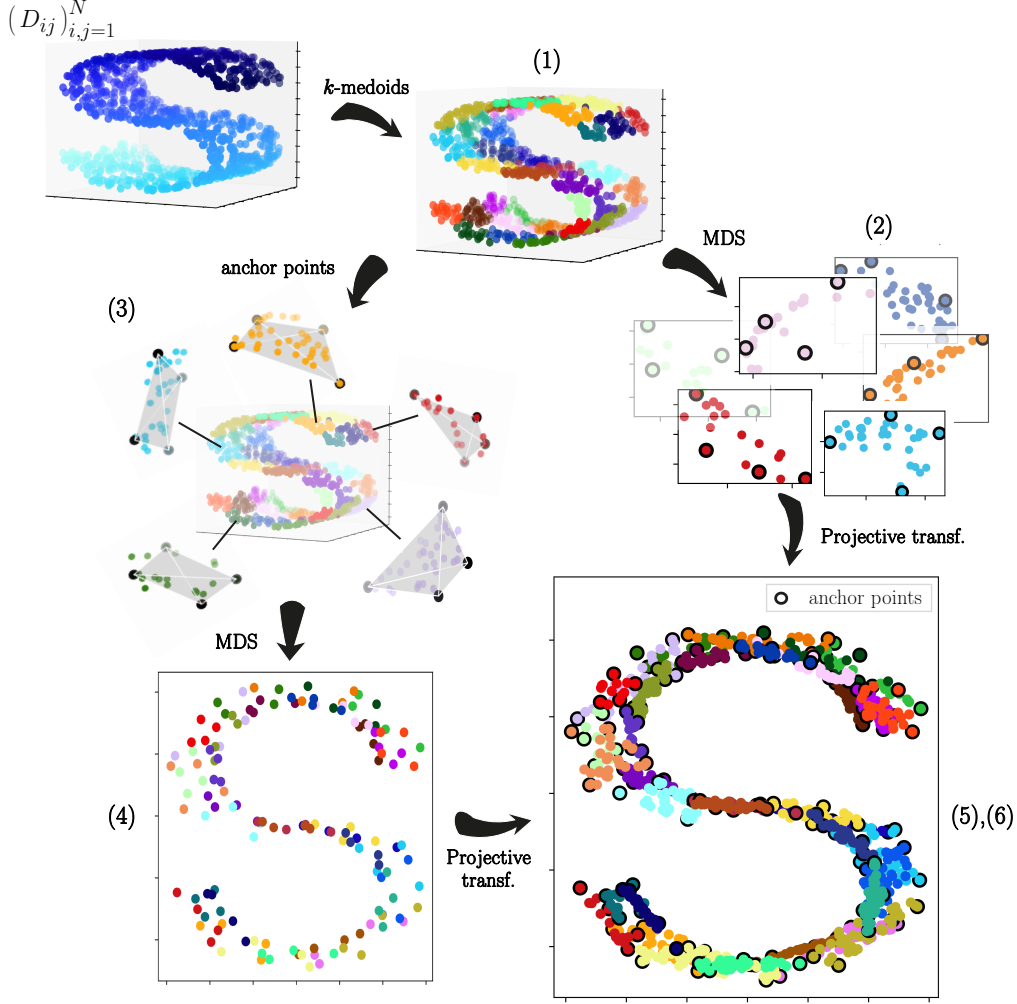


Figure 1: Steps of the cl-MDS algorithm: (1) k -medoids clustering of the data; (2) MDS-based local embedding of the individual clusters; (3) anchor-point selection within the individual clusters; (4) MDS-based global embedding of the anchor points only; (5,6) global embedding of all data points based on transformations derived from (2,4).

Since the division between local and global data structure is necessarily dataset-specific, we have extended the base cl-MDS algorithm outlined above to accommodate an arbitrarily complex nested hierarchy of the data structure. That is, the cl-MDS algorithm can perform an arbitrary number of levels of embedding, in practice usually limited to a few, by hierarchically grouping small clusters together into bigger ones. This feature can be useful for particularly complex datasets and is introduced in Section 2.4. Additional features of the algorithm are presented in Section 3, focused on a case application to representing atomic structures.

2.1 Local structures

The first part of cl-MDS seeks to identify all the local information present in the sample X . While there are global dimensionality reduction techniques, such as MDS, that in principle preserve most local structures, their performance significantly deteriorates as the size of X increases (see Section 4 for examples). We can ameliorate this problem by providing a sensible division of the sample into subsets of related data points and then computing a 2-dimensional embedding individually for each subset. Though it might seem that we are replacing one problem with another, this solution is quite convenient for our purposes as will become clear in the next subsections. Additionally, since the algorithm and its output are based on dissimilarity data, we have a natural criterion for a classification into subsets. Using that information, we can divide X in N_{cl} subsets known as *clusters*. Their main characteristic is the low dissimilarity values between members of a same cluster compared with those for points in different ones. As a result, each subset has a smaller distribution of dissimilarities than the complete sample, which will also help in our search for a finer embedding.

Therefore, the cl-MDS algorithm starts with the computation and optimization of a clustering of X (step 1), with the distance matrix \mathbf{D} and the total number of clusters N_{cl} as input parameters. A suitable clustering technique is the k -medoids method (Kaufman and Rousseeuw, 1987; Bauckhage, 2015), with $k = N_{\text{cl}}$ in our case. Unlike similar (and arguably more popular) barycenter-based algorithms such as k -means (Macqueen, 1967; Hartigan and Wong, 1979) or spectral clustering (Ng et al., 2001), k -medoids builds each cluster considering a *medoid*. This is the element in a cluster with minimal average dissimilarity to the remaining points in that same cluster. Thus, the k -medoids clustering process relies on selecting actual points from the sample as centroids, rather than these centroids being calculated as the coordinates in \mathbb{R}^n with, respectively, the smallest average intracluster distances. The distinction is important because, even though all points in X belong to \mathbb{R}^n , not all points in \mathbb{R}^n can necessarily be mapped back to a meaningful or interpretable data point. We will provide a concrete example of this lack of bijection in Section 3 for the smooth overlap of atomic positions (SOAP) high-dimensional representation of atomic structures (Bartók et al., 2013).

For computational efficiency, we have reimplemented Baukhage’s k -medoids Python recipe (Bauckhage, 2015) in Fortran. Our implementation, that we call **fast-kmedoids** (Caro and Hernández-León, accessed September 14, 2022b), can be easily built into a Python package with F2PY (Peterson, 2009). **fast-kmedoids** incorporates several other new features beyond increased speed, including optimization of initial medoid selection. The latter constitutes one of the main problems with centroid-based techniques, whose result heavily relies on the initialization. Since random selection is too volatile on its own, we combine it with *farthest point sampling* to select the `n_iso` most isolated points from the sample. By default, we set `n_iso` = 1. The complete clustering process in cl-MDS is performed as follows:

- 1.1 Use the k -medoids algorithm to obtain a set of clusters $\mathcal{C} = \{\mathcal{C}_1, \dots, \mathcal{C}_{N_{\text{cl}}}\}$ and their corresponding medoids $\mathcal{M} = \{m_1, \dots, m_{N_{\text{cl}}}\}$, where $m_k \in \mathcal{C}_k$, $\mathcal{C}_k \subset \mathcal{I}$ and $x_{m_k} \in X$ for any $k = 1, \dots, N_{\text{cl}}$.

1.2 Compute the relative intra-cluster *incoherence* (Caro et al., 2018),

$$I_{\text{rel}} = \sum_{k=1}^{N_{\text{cl}}} \frac{1}{N_{\mathcal{C}_k}} \left(\sum_{i \in \mathcal{C}_k} D_{i,m_k} \right), \quad (1)$$

where $N_{\mathcal{C}_k}$ denotes the cardinality of \mathcal{C}_k .

1.3 Repeat until a fixed maximum number of tries is reached, for a different medoid initialization. Keep the set with minimal I_{rel} , ensuring the lowest internal incoherence of the clusters among all candidate k -medoids solutions.

In our cl-MDS Python implementation (Caro and Hernández-León, accessed September 14, 2022a), the number of repetitions is set by the parameter `iter_med`, while the initialization of k -medoids is controlled by `init_medoids` and `n_iso_med`.

Next, we proceed with the embedding, step 2. A low-dimensional representation $Y_{\mathcal{C}_k}^{(l)}$ for each cluster \mathcal{C}_k is computed applying the standard MDS method, with $k = 1, \dots, N_{\text{cl}}$. In particular, we use a weighted variation (Caro and Hernández-León, accessed September 14, 2022a) of the metric MDS implementation included in the Python module `scikit-learn` (Pedregosa et al., 2011). In this version of the method, the coordinates in the low-dimensional space are optimized such that the pairwise distances between the embedded data points reproduce the input dissimilarity data as closely as possible. This is achieved by minimizing the stress, an objective function defined as

$$\sigma = \sum_i \sum_{i>j} w_{ij} (D_{ij} - d_{ij})^2, \quad (2)$$

where d_{ij} and w_{ij} correspond to the computed distances in the low-dimensional space and their weights respectively, with $i, j \in \mathcal{I}$. Therefore, each data point gets an optimized representation using a non-linear map. Note that we need to partition \mathbf{D} considering the previous set of clusters before computing the MDS embeddings; that is, each representation $Y_{\mathcal{C}_k}^{(l)}$ is obtained from a stress σ_k restricted to $i, j \in \mathcal{C}_k$.

Once step 2 concludes, a set of embeddings $Y^{(\text{local})} = \{Y_{\mathcal{C}_1}^{(l)}, \dots, Y_{\mathcal{C}_{N_{\text{cl}}}}^{(l)}\}$ is obtained. Hence, the output is a collection of N_{cl} 2-dimensional representations containing distinct “slices” of local information, despite reaching the same target space. As we will show next, they do not correspond to the final representation Y of our algorithm either.

2.2 Global structures

The second part of the cl-MDS algorithm gathers the global information and maps it to a 2-dimensional space \mathbb{R}^2 . As for the local embeddings, we utilize the same dimensionality reduction technique, MDS. As we discussed in Section 2.1, MDS mapping of the whole sample may lead to unsatisfactory results for large datasets, whereas applying it to a small subset made of selected points could give us enough insight into its global features. That subset must also contain several reference points from each cluster, enclosing as much local information as possible. Since the distribution of those points also determines the global map, they will act as *anchor points* between local and global representations. Therefore,

this part of cl-MDS is divided in two steps: finding a suitable collection of reference points that “frames” all clusters (step 3) and, then, proceeding with their embedding (step 4).

Step 3 selects as anchor points a subset of X aiming at satisfying two conditions simultaneously: preserving a maximal amount of local information and outlining the overall sample features. Intuitively, we need at least one anchor point from each cluster to grasp their global distribution. However, this would disregard the local structure within the clusters. Therefore, in practice, up to four anchor points per cluster ($1 \leq n_{\text{anc}} \leq 4$) are chosen to both ensure the aforementioned preservation of local features and ease the MDS minimization problem. The benefits of this choice are further discussed on Section 2.3. Hence, this part of the algorithm searches the high-dimensional representation of each cluster \mathcal{C}_k for the vertices $\mathcal{A}_k = \{a_{k1}, \dots, a_{kn_{\text{anc}}}\} \subset \mathcal{C}_k$ which define the tetrahedron of maximal volume, for $k = 1, \dots, N_{\text{cl}}$. The detailed procedure is as follows:

- 3.1 Check if the cardinality $N_{\mathcal{C}_k}$ of cluster \mathcal{C}_k satisfies $N_{\mathcal{C}_k} > N_{\mathcal{C}_k}^{\text{max}}$. For the sake of computational efficiency, large clusters benefit from discriminating between points to reduce the list of candidate vertices before considering any tetrahedra. In that case, the p -th percentile of the distance to the medoid m_k is chosen as threshold, leaving only farther points in \mathcal{C}_k as vertices. The percentile rank p is customized for different $N_{\mathcal{C}_k}$ with the parameter `param_anchor`. Our tests indicate that $N_{\mathcal{C}_k}^{\text{max}} = 70$ is a robust choice, and this is hardcoded in the cl-MDS program.
- 3.2 Compute the volume of each possible tetrahedron whose vertices v are a subset of the (reduced) list of points in \mathcal{C}_k . Since a tetrahedron corresponds to a 3-simplex S_3 , its volume V can be computed using the Cayley–Menger determinant as follows (Sommerville, 1929; Gritzmann and Klee, 1994):

$$V(S_3)^2 = \frac{1}{2^3(3!)^2} \begin{vmatrix} 0 & \mathbf{1}_4^\top \\ \mathbf{1}_4 & \mathbf{D}[v] \end{vmatrix}, \quad (3)$$

where $\mathbf{1}_4^\top = (1, 1, 1, 1)$ and $\mathbf{D}[v]$ is the 4×4 submatrix of \mathbf{D} corresponding to the vertices of the 3-simplex. We note here that the tetrahedron’s volume is computed directly from the distances, and that these distances are not necessarily based on an Euclidean metric.

- 3.3 Keep the set of vertices \mathcal{A}_k forming the tetrahedron with maximal volume.

Repeating those steps for each cluster, we obtain the complete set of anchor points $\mathcal{A} = \bigcup_{k=1}^{N_{\text{cl}}} \mathcal{A}_k$. We opted for the volume as a measure of the amount of preserved information, although one could argue that there exist better criteria, such as the number of data points enclosed by the tetrahedron. Those measures are nonetheless much more expensive computationally given their dependence on $N_{\mathcal{C}_k}$, whereas the volume criterion is independent of it.

Finally, step 4 is carried out. Applying the same weighted metric variation of the MDS method from step 2, a 2-dimensional representation of the anchor points $Y_{\text{anchor}}^{(\text{g})} = \{y_{a_i}^{(\text{g})} \mid a_i \in \mathcal{A}\}$ is computed. Notably, those new coordinates encode the global 2-dimensional distribution of the local structures previously clustered.

2.3 From local to global embedding

We have so far obtained a *collection* of low-dimensional representations of the original dataset X , characterized by preserving local and global structures *separately*. These embeddings are limited to certain subsets of points, i.e., anchor points in the case of the global one and clusters in the case of the local ones. The last part of the algorithm seeks to reconcile these two independent representations to achieve a complete representation Y of X , by mapping each cluster’s local coordinates into the global map. That is, given a cluster \mathcal{C}_k with $k = 1, \dots, N_{\text{cl}}$, we can leverage its anchor points \mathcal{A}_k , whose coordinates are known in local and global representations, to obtain a suitable transformation for all of its members.

Two types of transformations are implemented: affine transformations \mathbf{A} , and projective transformations \mathbf{H} (also known as perspective mappings or *homographies*) (Schneider and Eberly, 2003). The simpler affine transformations preserve parallel lines, as opposed to the non-linear maps performed by the MDS algorithm. Hence, homographies were introduced for the sake of consistency, since they always preserve incidence (relations of containment between points, lines and planes) but not parallelism. There are other properties that are not preserved by the MDS algorithm, suggesting that there is room for future improvement in this direction. For instance, the relative ordering of distances between points is not always preserved, despite the MDS efforts of reproducing relative distances [see Eq. (2)]. This property will influence the selection process in step 5, as we explain below.

Before computing a transformation operator (in the form of a matrix), we need to ensure the absence of pathological configurations. Step 5 determines the most suitable transformation (affine or projective) for each cluster, depending on the number of anchor points n_{anc} and their relative distribution in both representations. The importance of this last property lies in its relation to convexity, which is a necessary (and sufficient) condition for homography. That is, the anchor points \mathcal{A}_k ($k = 1, \dots, N_{\text{cl}}$) form a quadrilateral in each representation whose convexity is not ensured in both maps (as anticipated above), potentially leading to an ill-conditioned transformation. Thus, the pathology check for a cluster \mathcal{C}_k is performed as follows:

- 5.1 Check if $n_{\text{anc}} < 4$. In that case, an affine transformation $\mathbf{A}_{\mathbf{k}}$ is chosen trivially and no further steps are needed.
- 5.2 Check if \mathcal{A}_k does not coincide with its convex hull (i.e., the smallest convex subset in \mathcal{A}_k containing \mathcal{A}_k) in the local representation $Y_{\mathcal{A}_k}^{(l)}$. This corresponds to one of the anchor points being enclosed within the triangle defined by the other three, or to (at least) three anchor points being collinear. In that case, a homography is ill-conditioned and we redefine \mathcal{A}_k as its convex hull, implying $n_{\text{anc}} < 4$ and obtaining the result of step 5.1. The convex hull is computed using the Qhull library (Barber et al., 1996) through `scipy.spatial.ConvexHull` (Virtanen et al., 2020).
- 5.3 Repeat the previous check, now using the global representation $Y_{\mathcal{A}_k}^{(g)}$. If true, the four anchor points will be used to compute an affine transformation $\mathbf{A}_{\mathbf{k}}$. Otherwise, the convexity is confirmed in both representations and a homography $\mathbf{H}_{\mathbf{k}}$ is chosen.

Once each cluster has been checked, the algorithm can proceed with their mapping using the most appropriate transformation $\mathbf{T}_{\mathbf{k}}$ for each $k = 1, \dots, N_{\text{cl}}$, where $\mathbf{T}_{\mathbf{k}}$ corresponds to

\mathbf{A}_k or \mathbf{H}_k . For simplicity, we use homogeneous coordinates to express the details of step 6. In this notation, any point $p^\top = (x, y)$ from \mathbb{R}^2 has an homogeneous representation $\tilde{p}^\top = (x, y, 1)$. On the other hand, any homogeneous point $\tilde{q}^\top = (u, v, w)$ is identified with $\tilde{r}^\top = \tilde{q}^\top/w = (u/w, v/w, 1)$, implying the existence of a bijection between cartesian coordinates in the Euclidean plane and homogeneous coordinates in the *projective plane* (\mathbb{P}^2). Alternatively, equivalence classes can be used to understand the concept of homogeneous coordinates within a more rigorous theoretical framework (Richter-Gebert, 2010). This notation allows us to represent the transformations as simple matrix multiplications, whose details are explained below. Then, step 6 is organized as follows:

6.1 Compute the transformation matrix \mathbf{T}_k that solves the equation

$$\begin{pmatrix} y_{a_i}^{(g)} \\ 1 \end{pmatrix} = \mathbf{T}_k \begin{pmatrix} y_{a_i}^{(l)} \\ 1 \end{pmatrix}, \quad (4)$$

for each $a_i \in \mathcal{A}_k$.

In particular, affine transformations (usually represented as the composition of a linear transformation \mathbf{L}_k and a translation \mathbf{b}_k) correspond to the following matrix,

$$\mathbf{A}_k = \begin{pmatrix} \mathbf{L}_k & \mathbf{b}_k \\ \mathbf{0}_n^\top & 1 \end{pmatrix}, \quad (5)$$

where $\mathbf{0}_2^\top = (0, 0)$ for transformations in \mathbb{R}^2 , and, therefore, they are obtained as the least-squares solution of Eq. (4).

On the other hand, a homography matrix (Eberly, Accessed September 14, 2022) has the form

$$\mathbf{H}_k = \left(\mathbf{A}_k^{(g)} \right)^{-1} \mathbf{F} \mathbf{A}_k^{(l)}, \quad (6)$$

where $\mathbf{A}_k^{(l)}$ is the affine transformation from the local \mathcal{A}_k coordinates to the *canonical quadrilateral* $\{(1, 0), (0, 0), (0, 1), (a, b)\}$, with $(a, b) = \mathbf{A}_k^{(l)} y_{a_3}^{(l)}$. Likewise, $\mathbf{A}_k^{(g)}$ is the equivalent transformation from the global coordinates to a canonical quadrilateral whose fourth point is $(c, d) = \mathbf{A}_k^{(g)} y_{a_3}^{(g)}$. Both affine transformations can be computed using the least-squares method too. Finally, \mathbf{F} is a *linear fractional transformation* from the first canonical quadrilateral into the second,

$$\mathbf{F} = \begin{pmatrix} bcs & 0 & 0 \\ 0 & ads & 0 \\ b(cs - at) & a(ds - bt) & abt \end{pmatrix}, \quad (7)$$

where $s = a + b - 1$ and $t = c + d - 1$ are positive for convex quadrilaterals. Since both pairs (a, b) and (c, d) are known from the previous affine transformations, \mathbf{F} is known too.

6.2 Compute the global representation of cluster \mathcal{C}_k using the previous mapping,

$$\begin{pmatrix} y'_i \\ w \end{pmatrix} = \mathbf{T}_k \begin{pmatrix} y_i^{(l)} \\ 1 \end{pmatrix}, \quad (8)$$

and applying the *perspective divide* $y_i^{(g)} = y'_i/w$ to each $i \in \mathcal{C}_k$.

6.3 If $\mathbf{T}_k = \mathbf{H}_k$, an affine transformation is also computed for comparison. We retain the result with the lowest residue,

$$R(\mathbf{T}_k) = \sum_i (y_i^{(l)} - y_i^{(g)}(\mathbf{T}_k))^2, \quad (9)$$

in order to minimize the effect of outliers.

As a result of step 6, we obtain the output of the cl-MDS algorithm, $Y = \bigcup_{k=1}^{N_{cl}} Y_{C_k}^{(g)} = \{y_1, \dots, y_N\}$. These steps constitute the core of the cl-MDS algorithm.

2.4 Cluster hierarchy and sparsification

Additional features are implemented to complement and improve the cl-MDS algorithm. Here we introduce the general ones, whereas Section 3 details those specific to visualization of databases of atomic structures. While cl-MDS strives to preserve local and global structures, its base algorithm sometimes lacks the sufficient flexibility for mapping complex databases where different layers of locality can be meaningful. To address this issue we introduce *cluster hierarchy*. In a hierarchical cluster setup, the number of clusters hyperparameter N_{cl} is replaced by a hierarchy hyperparameter,

$$h = [N_{\text{level } 0}, N_{\text{level } 1}, N_{\text{level } 2}, \dots, 1], \quad (10)$$

where $N_{\text{level } 0}$ refers to the finest clustering level and 1 represents the final global MDS embedding (i.e., $N_{\text{level } 0} > \dots > N_{\text{level } m} > \dots > 1$). This list enables a hierarchical embedding on steps 3 to 6 that mimics the idea behind hierarchical clustering (Hastie et al., 2009). Each level m corresponds to a grouping $\mathcal{C}^{(m)}$ of the dataset with a specific embedding $Y^{(m)}$ in the 2-dimensional Euclidean space, such that the next level $(m+1)$ merges several of those clusters and computes a new 2-dimensional embedding $Y^{(m+1)}$, using $Y^{(m)}$ as the local representation. In this way, hierarchical embedding improves the representation of samples with several levels of locality. The simplest hierarchy $[N_{cl}, 1]$ is equivalent to N_{cl} , where a sole layer of local information is considered. The hierarchy approach is schematically depicted in Fig. 2 for a [5,2,1] hierarchy. See Section 4 for examples.

To enable processing of large databases we have added sparsification support to cl-MDS. In our Python implementation this is selected through the keywords `sparsify` and `n_sparse`. Sparsification carries out the cl-MDS operations only on a subset of the data points, selected according to some predefined recipe (`sparsify = "random" | "cur" | list`). `n_sparse` determines the (maximum) size of the resulting sparse set, denoted \mathcal{I}_{sp} . Three sparsification options are implemented. The first selection method, "random", uses `numpy`'s random sampling routines (Harris et al., 2020). The second option, "cur", is based on CUR matrix decomposition (Drineas et al., 2006; Mahoney et al., 2008), a low-rank approximation procedure. This decomposition is characterized by retaining those rows (and columns) from the original matrix that allow its best low-rank fit, i.e., that capture the most representative part of it. The "significance" of a row can be expressed in terms of its statistical influence (Mahoney and Drineas, 2009) or its Frobenius norm (Leskovec et al., 2020), among other properties. The CUR implementation included in cl-MDS uses the latter. Hence, given a distance matrix \mathbf{D} and a rank `n_sparse`, we choose the indices of

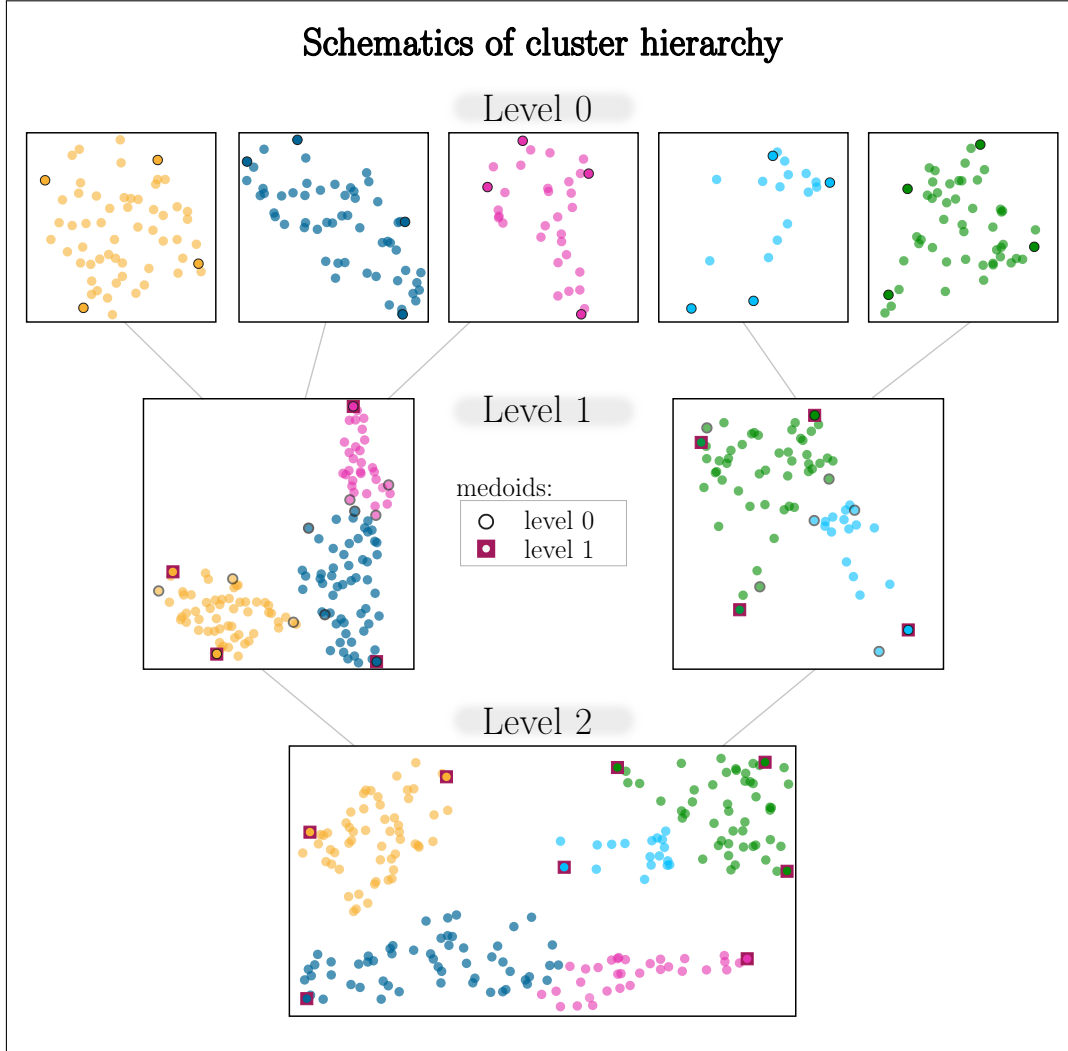


Figure 2: Illustration of the hierarchical cluster setup, using a $[5, 2, 1]$ hierarchy. The figure includes the set of anchor points obtained per clustering level, following step 3. The last level does not require such set since it corresponds to the final embedding.

those rows with higher Frobenius norm within the dataset. As a third sparsification option, the user can provide directly a custom list or array with the sparse indices to `sparsify`.

Bearing sparsification in mind, we developed a supplementary algorithm (step 7) that estimates the low-dimensional representation of those data points not included in the sparse set, i.e., $\bar{\mathcal{I}}_{sp} := \mathcal{I} - \mathcal{I}_{sp}$. The embedding transformations inferred for the sparse set are reused for embedding $\bar{\mathcal{I}}_{sp}$, whereas the MDS mapping per cluster is replaced by an affine mapping. This is achieved through a three-step process:

- 7.1 Assign each data point i in $\bar{\mathcal{I}}_{sp}$ to the same cluster \mathcal{C}_k as its nearest medoid m_k , with $k \in \{1, \dots, N_{cl}\}$. This approach extends the existing clustering to the complete

database without requiring computing or storing its complete distance matrix. To avoid future confusion, we refer to the extended cluster k as \mathcal{C}_k^* , implying that $\mathcal{C}_k = \mathcal{C}_k^* \cap \mathcal{I}_{sp}$.

- 7.2 Compute an affine mapping from the original high-dimensional space \mathbb{R}^n to \mathbb{R}^2 , for each cluster \mathcal{C}_k^* with $k = 1, \dots, N_{cl}$. Its matrix representation $\tilde{\mathbf{A}}_k$ is the least-squares solution to the equation

$$\begin{pmatrix} y_j^{(l)} \\ 1 \end{pmatrix} = \tilde{\mathbf{A}}_k \begin{pmatrix} x_j \\ 1 \end{pmatrix}, \quad (11)$$

for all sparse points $j \in \mathcal{C}_k$. The tilde is included to emphasize that the embedding is between distinct spaces, as opposed to the affine transformations from step 6.

- 7.3 Obtain the 2-dimensional representation of each cluster \mathcal{C}_k^* via the composition $\tilde{\mathbf{T}}_k := \mathbf{T}_k \tilde{\mathbf{A}}_k$, with $k = 1, \dots, N_{cl}$. Similarly to step 6.2, these coordinates are the result of the perspective divide $y_i^{(g)} = y'_i/w$, defined by the equation

$$\begin{pmatrix} y'_i \\ w \end{pmatrix} = \tilde{\mathbf{T}}_k \begin{pmatrix} x_i \\ 1 \end{pmatrix}, \quad (12)$$

where $i \in \mathcal{C}_k^* \cap \bar{\mathcal{I}}_{sp}$. Note that we exclude the data points from \mathcal{C}_k from these calculations because their 2-dimensional representation is already known.

Therefore, this algorithm completes the 2-dimensional representation of the database, $Y = \{y_1, \dots, y_N\}$, previously restricted to the sparse set, $Y_{sp} := \{y_j \mid j \in \mathcal{I}_{sp}\}$. Note that the estimation will be as good (or as bad) as the chosen sparse set.

3. Embedding atomic structure representations

Analyzing atomic databases, which can comprise thousands (even millions) of structures, has become an increasingly difficult task. During the last decade, new mathematical descriptions of atomic structures have been developed as an alternative to simpler approaches, such as straightforward visualization of the structures, which are prone to information overload from such databases. As a result, we can compare their members (either atoms or molecules) using abstract mathematical representations known as *atomic descriptors* (Bartók et al., 2013; Willartt et al., 2019; De et al., 2016), where each member is characterized numerically. This representation ranges from simple scalar distances and angles to complicated many-body atomic descriptors which are mapped to high-dimensional vectors. These representations can be used to compute a similarity measure between atomic configurations based on kernel functions, paving the way to study these databases and their underlying properties. Still, the dimensionality of these descriptions can obscure the results and their communication, as we discussed in Section 1.

The high-dimensional nature of many-body atomic representations makes them a representative example of the usefulness of dimensionality reduction techniques, in general, and cl-MDS, in particular. These methods can be very effective for visually comparing atomic structures and studying patterns within a database, fostering the development of related

software (Ceriotti et al., 2011; De and Ceriotti, 2019; Fraux et al., 2020; Cheng et al., 2020) in recent years. Some of the most common techniques adopted by materials scientists are the linear algorithm PCA, its non-linear counterpart kernel PCA (kPCA) (Schölkopf et al., 1998), metric MDS, and, more recently, diffusion maps (Coifman et al., 2005; Coifman and Lafon, 2006). As already mentioned in Section 1, they fail to simultaneously preserve global and local features, a key property to obtain a meaningful visualization of these databases where several structural relations are present at different scales.

We have added functionality to the cl-MDS code specifically tailored for processing atomic structure information. First, the distance matrix \mathbf{D} can be substituted by a file as input parameter, given in a format compatible with the Atomic Simulation Environment (ASE) Python library (Bahn and Jacobsen, 2002; Larsen et al., 2017). This file may include a single atomic structure, a concatenation of them, or a trajectory. Given this input, the user also selects a representation for the atomic descriptors, which are automatically computed by the cl-MDS code. Currently, there are two supported options (`descriptor = "quippy_soap" | "quippy_soap_turbo"`) available via `quippy`, a Python interface to the Fortran code QUIP (Csányi et al., 2007) generated by `f90wrap` (Kermode, 2020). The first option, "quippy_soap", describes atomic environments using the smooth overlap of atomic positions (SOAP) vectors (Bartók et al., 2013). This many-body representation incorporates the required symmetries for a consistent comparison between structures, namely invariance under translations, rotations and permutations of identical atoms. Within this framework, the atomic density field surrounding an atom i is defined as a smooth sum of the contributions from individual neighbors j ,

$$\rho^{(i)}(\mathbf{r}) = \sum_{j \in S_i} \rho_j(\mathbf{r}) = \sum_{j \in S_i} \exp\left(-\frac{(\mathbf{r} - \mathbf{r}_j)^2}{2\sigma^2}\right), \quad (13)$$

where S_i denotes the sphere centered on atom i with a fixed cutoff radius (i.e., the *atomic neighborhood* of atom i , which includes i itself), and $\rho_j(\mathbf{r})$ corresponds to a 3-dimensional Gaussian centered on atom j . This field is in practice expanded in terms of an orthonormal radial basis $\{g_n\}$ and spherical harmonics $\{Y_{lm}\}$ as

$$\rho^{(i)}(\mathbf{r}) = \sum_{nlm} c_{nlm}^i g_n(r) Y_{lm}(\theta, \phi). \quad (14)$$

The expansion coefficients c_{nlm}^i define a set of invariants $\mathbf{p}_i := \{p_{nn'l}^i\}$, where each quantity

$$p_{nn'l}^i = \sum_m c_{nlm}^i (c_{n'lm}^i)^* \quad (15)$$

is known as the *power spectrum*. Finally, the corresponding normalized vectors define the SOAP atomic descriptors,

$$\mathbf{q}_i^{\text{SOAP}} := \frac{\mathbf{p}_i}{|\mathbf{p}_i|}, \quad (16)$$

for each atom i in the database. The option "quippy_soap_turbo" uses an optimized version of the SOAP atomic descriptors from Eq. (16) through the `soap_turbo` library (Caro,

accessed September 14, 2022, 2019). This framework assumes a separable form for the atomic density $\rho_j(\mathbf{r})$ defined on Eq. (13), approximating it by a radial and angular part:

$$\rho_j(\mathbf{r}) \approx \exp\left(-\frac{(r-r_j)^2}{2\sigma_r^2}\right) \exp\left(-\frac{r_{\perp,j}^2}{2\sigma_{\perp}^2}\right). \quad (17)$$

We refer the reader to Ref. (De et al., 2016) for an extension of SOAP to handling multiple species.

A string of hyperparameter definitions can be given for both descriptor options (`descriptor_string`). Alternatively, the user can simply choose a cutoff radius and rely on the code defaults. Other implemented options include `average_kernel`, which extends the previous mathematical representations to whole structures (only available with "quippy-soap"); and `do_species`, which allows the pre-selection of certain species within a database to speed up the calculations. The user can also provide an array of precomputed descriptors obtained with an external tool, such as `DScRibe` (Himanen et al., 2020).

Once we have a representation of the atomic structures, we need to obtain its associated distance matrix. A suitably constructed atomic descriptor provides the basis for defining a metric that can be fed into the cl-MDS algorithm. That is, it can be proven that these vectors lead to a positive-definite kernel with an induced Gram matrix \mathbf{K} of size $N \times N$, where N is the length of the database. For SOAP this kernel function is defined as (Bartók et al., 2013)

$$K_{ij} = (\mathbf{q}_i^{\text{SOAP}} \cdot \mathbf{q}_j^{\text{SOAP}})^{\zeta}, \quad (18)$$

where ζ can be any positive scalar and $0 \leq K_{ij} \leq 1$. The importance of defining a kernel resides in its connection with a dissimilarity measure. As shown in Ref. (Schölkopf, 2000), it is always possible to find a dissimilarity measure \mathbf{D} associated to a positive definite kernel \mathbf{K} , given by

$$(D_{ij})^2 = \frac{1}{2}(K_{ii} + K_{jj}) - K_{ij}. \quad (19)$$

Considering Eq. (16) and Eq. (18), the resulting dissimilarity matrix is

$$D_{ij} = \sqrt{1 - K_{ij}}. \quad (20)$$

This distance measure is automatically computed by the cl-MDS code from the set of atomic descriptors prior to performing the clustering and embedding steps.

In addition to the embedding features described in Section 2.4, we have also added the possibility of fine-tuning the minimization process of the MDS stress from step 4 (see Section 2) by means of a weighted distance matrix. While our MDS implementation can generally accommodate weights, this is a straightforward extension for atomic structure visualization based on the SOAP kernel, which is evaluated for the set of medoids \mathcal{M} . That is, given two atoms $i \in \mathcal{C}_k$, $j \in \mathcal{C}_s$ and a positive integer η , the distance is redefined as

$$D_{ij}^{(w)} = \sqrt{1 - K_{ij} \cdot (K_{m_k, m_s})^{\eta}}. \quad (21)$$

Thus,

$$\mathbf{D}^{(w)} = [1 - \mathbf{K} \odot (\mathbf{K}_{\mathcal{M}})^{\odot \eta}]^{1/2}, \quad (22)$$

where \odot denotes the element-wise product (also known as Hadamard or Schur product) and element-wise exponentiation, and

$$\begin{aligned} (K_{\mathcal{M}})_{ij} &= K_{m_k, m_s}, & \text{if } i \in \mathcal{A}_k \text{ and } j \in \mathcal{A}_s, \\ (K_{\mathcal{M}})_{ij} &= 1, & \text{if and only if } i, j \in \mathcal{A}_k. \end{aligned}$$

These weighted distances allow us greater control in decoupling the representation of individual clusters on the global map, effectively allowing us to continuously increase the emphasis on the local vs global structure of the data.

4. Examples

In this section, we analyze several examples to show the potential of the cl-MDS method as well as its weaknesses. First, a variety of toy examples are introduced in Section 4.1 to illustrate its main features and to compare its performance with other dimensionality reduction techniques. Instances of higher complexity are shown in Sections 4.2 and 4.3, regarding two extensive atomic databases: the structural database of materials containing carbon, hydrogen and oxygen (CHO) from Ref. (Golze et al., 2022) and the database of small molecules QM9 (Ruddigkeit et al., 2012; Ramakrishnan et al., 2014). Additional details of these datasets are given in their respective sections. We decided to focus on atomic-structure samples because (i) they were our motivation to develop cl-MDS in the first place, and (ii) we wanted to apply all the functionalities previously mentioned, including those related to atomic structure representations. However, the cl-MDS method is applicable to datasets from other fields too.

The following algorithms are considered for qualitative comparisons with cl-MDS: locally linear embedding (LLE) (Roweis and Saul, 2000), modified LLE (Zhang and Wang, 2007), Hessian eigenmaps (Hessian LLE) (Donoho and Grimes, 2003), local tangent space alignment (LTSA) (Zhang and Zha, 2002), Laplacian eigenmaps (LE) (Belkin and Niyogi, 2003), and the already mentioned Isomap (Tenenbaum et al., 2000), PCA (Hotelling, 1933), kPCA (Schölkopf et al., 1998), MDS (Kruskal, 1964a,b), t-SNE (van der Maaten and Hinton, 2008; van der Maaten, 2014) and UMAP (McInnes et al., 2020). They are computed using `scikit-learn` (Pedregosa et al., 2011) implementations except for UMAP, which has its own Python module (`umap`). On the other hand, detailed quantitative comparisons (the so-called goodness-of-fit tests) are not included, since a good choice of metric is highly dependent on the application domain, the user’s expectations and the sample itself (Bertini et al., 2011). These metrics are (inevitably) tailored to diverse definitions of accuracy and visual quality, further adapted to account for specific shortcomings (e.g., the DEMaP metric (Moon et al., 2019), the “local continuity” (LC) meta-criteria (Chen and Buja, 2009), or measures of *trustworthiness* and *continuity* (Venna and Kaski, 2006)). Therefore, we opted for strong qualitative comparisons that provide a broader taste of cl-MDS, but we encourage the user to apply these metrics to their own samples after careful selection.

As a consequence of its algorithm, cl-MDS inherits several characteristics of MDS which are relevant for understanding the figures in this section. While their embedding dimensions

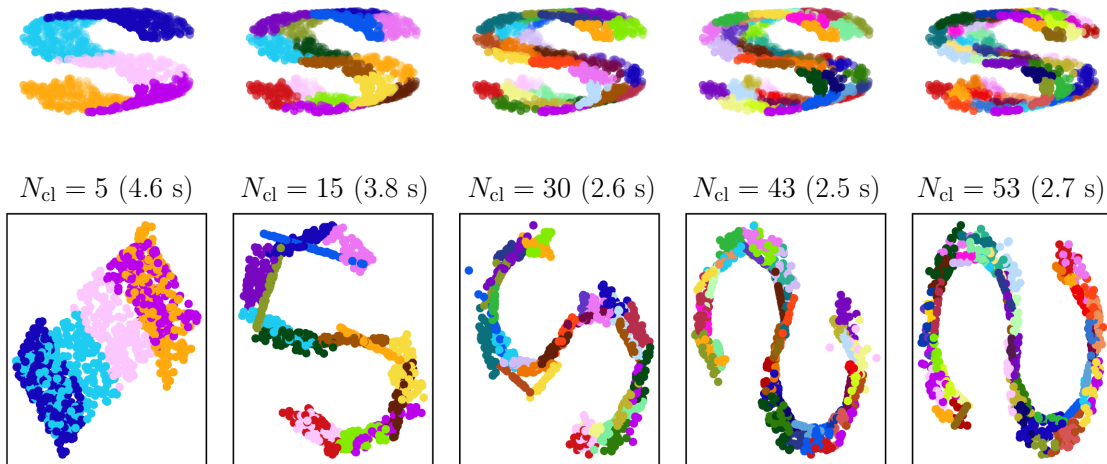


Figure 3: Effect of the number of clusters N_{cl} in cl-MDS embedding and performance for a simple example.

lack interpretability (i.e., absence of meaningful axes), the relative Euclidean distances of the resulting 2-dimensional representation encode the original dissimilarity measure. Thus, the nearer two data points are in this visualization, the more similar they are and vice versa. In practice, this does not always hold for MDS, a problem that cl-MDS alleviates as we will discuss in Section 4.2. Additionally, the embedded representation is invariant under affine transformations for both methods. However, the embedding codomain of cl-MDS is usually $[-1, 1] \times [-1, 1]$ without being strictly restricted to it, as opposed to MDS. Since dimensionality reduction techniques differ on their codomain, as well as on their interpretation (only PCA has a strong meaning associated to its axes), we omit the axis information in all the figures to avoid misleading comparisons.

4.1 Toy examples

Before diving into complex examples, let us discuss the main features of cl-MDS using simpler datasets. We start following a classic `scikit-learn` example of manifold learning methods (Vanderplas, accessed September 14, 2022), where an S-curve dataset with 1000 points and its corresponding Euclidean distances are used. We chose minimal parameters for all the techniques to compare their fastest computational speed. However, note that cl-MDS was not intended for improving time performance and has not been fully optimized accordingly. Also, this is the only example where the parameters are not fine tuned.

Figure 3 illustrates the effect of the cl-MDS main hyperparameter, the number of clusters N_{cl} (see Section 2.1). As expected, the algorithm output is sensitive to this choice, requiring a minimum clustering ($N_{cl} = 15$) to preserve the distances in the embedded space consistently. Just like MDS, cl-MDS focuses on revealing the metric structure, which does

not guarantee uncovering the low-dimensional manifold. This is especially true when using Euclidean distances, since they do not characterize the global distribution of the manifold properly. Hence, this particular example requires feeding a larger amount of local information to the global MDS mapping (step 4) through the clustering, in order to counteract the ambiguity in large distances.

In general, a good choice of N_{cl} depends on the database and the provided metric, although a number between 5 and 20 is enough in our experience to capture local and global details properly. A higher number of clusters can be useful to retrieve finer details, especially in highly complex datasets. Nevertheless, overly increasing N_{cl} worsens the global embedding and dilutes the intrinsic value of medoids as representative data points. Therefore, we recommend finding a compromise between a finer embedding and a smaller clustering. In particular cases, a carefully devised cluster hierarchy can prove quite helpful; the added versatility of hierarchy and medoids information will be discussed in depth in Sections 4.2 and 4.3. Although we use a heuristic approach for fine-tuning all the parameters in this article, there are well-known criteria for choosing a suitable number of clusters (Liu et al., 2010; Halkidi et al., 2001). We have already explored some options, such as the elbow method and the silhouette statistic (Kaufman and Rousseeuw, 1990), but further analysis is needed in this direction.

On the other hand, the performance of cl-MDS improves timewise with the number of clusters, being even faster than MDS for $N_{cl} > 15$ (see MDS performance in Fig. 4). While counter-intuitive at first, this result illustrates the usual trade-off between performance and sample size already mentioned in Section 2.1. Although the cl-MDS algorithm uses several instances of MDS, the subset of data points processed per instance is much smaller than the complete sample. As Fig. 3 shows, increasing N_{cl} decreases average cluster size and speeds up individual cl-MDS calculations, until it reaches a threshold ($N_{cl} > 43$ in this example). This threshold is determined by the set of anchor points, whose size grows approximately as $4N_{cl}$, recovering the previous tradeoff. Thus, we conclude that our initial/previous compromise for choosing N_{cl} is also reasonable in terms of performance.

Note that, once a suitable N_{cl} is reached, bigger clusterings may better incorporate the nuanced local details and improve its visual quality, but they do not change the overall embedding significantly. This is a fundamental distinction between cl-MDS and those methods whose main hyperparameter fixes (or guesses) the *number of close neighbors* for each point, i.e., the locality of the embedding. Fig. 4 shows examples of the latter in its first two rows. Most of these methods aim to embed the original data uniformly, as opposed to the techniques included in the last row which seek to preserve the metric structure. That is, the former obtain an isotropic representation of the S-manifold but the metric information is partially lost.

Additional cl-MDS parameters, such as the MDS weights and the percentile ranks for anchor points, were minimized here for increased computational speed, reducing the accuracy too. In Fig. 3, we can appreciate the extreme linearity of certain cluster embeddings, which translates into the cl-MDS mapping being slightly less accurate than the MDS one in Fig. 4. This effect is a consequence of the MDS optimization process, which does not guarantee the preservation of relevant incidence relations (e.g., placing anchor points from the same cluster, originally convex, on a line). Moreover, this is accentuated by a high number of clusters, poor choices of anchor points and insufficient MDS iterations. To alleviate this

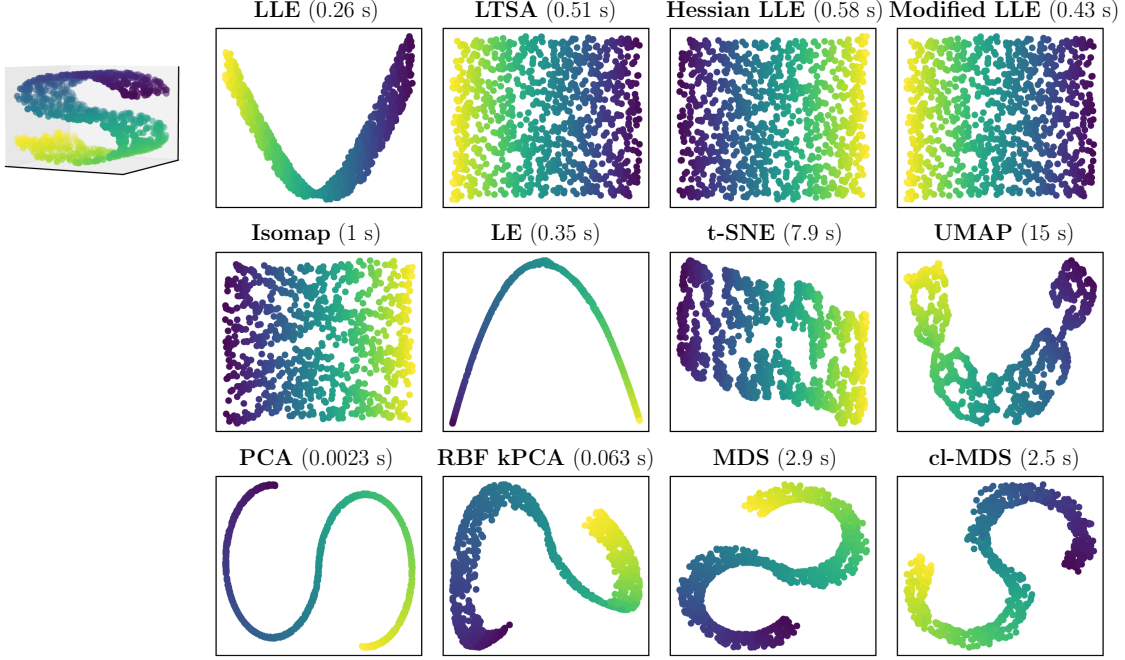


Figure 4: Comparison of several dimensionality reduction techniques applied to an S-curve manifold with 1000 points. Like the original example (Vanderplas, accessed September 14, 2022), we used minimal parameters whenever possible. The top two rows include those methods that require a fixed number of neighbors, in this case limited to 15.

issue, the cl-MDS implementation includes optimized values of all related parameters by default, reducing the emergence of these artifacts.

The next example corresponds to a dataset of 1000 random points distributed over the unit square, avoiding N_h randomly placed circular regions (*holes*). Rather than characterizing each point i by its 2-dimensional coordinates, we use the vector $v_i := (d_{i h_1}, \dots, d_{i h_{N_h}}) \in \mathbb{R}^{N_h}$ where $d_{i h_j}$ denotes its Euclidean distance to the center of the hole h_j , for $j = 1, \dots, N_h$. This is a straightforward approach for building a high-dimensional dataset with a custom dimension N_h . Figure 5 illustrates this for an $N_h = 12$ example, with the pairwise distances in \mathbb{R}^{12} fed to cl-MDS. Additionally, this figure includes an application of Voronoi diagrams as a qualitative measure of accuracy for cl-MDS. The Voronoi partition of a set of points corresponds to those regions of space, *Voronoi cells*, containing the closest generator point. That is, the Voronoi partition associated to the medoids in \mathbb{R}^{12} is equivalent, by definition, to clustering these medoids in this Euclidean space. Hence, the metric topology on this partition is preserved in the 2-dimensional embedding only when the Voronoi cells in \mathbb{R}^2 contain the clusters perfectly. Figure 5 shows how close cl-MDS is to achieving this objective.

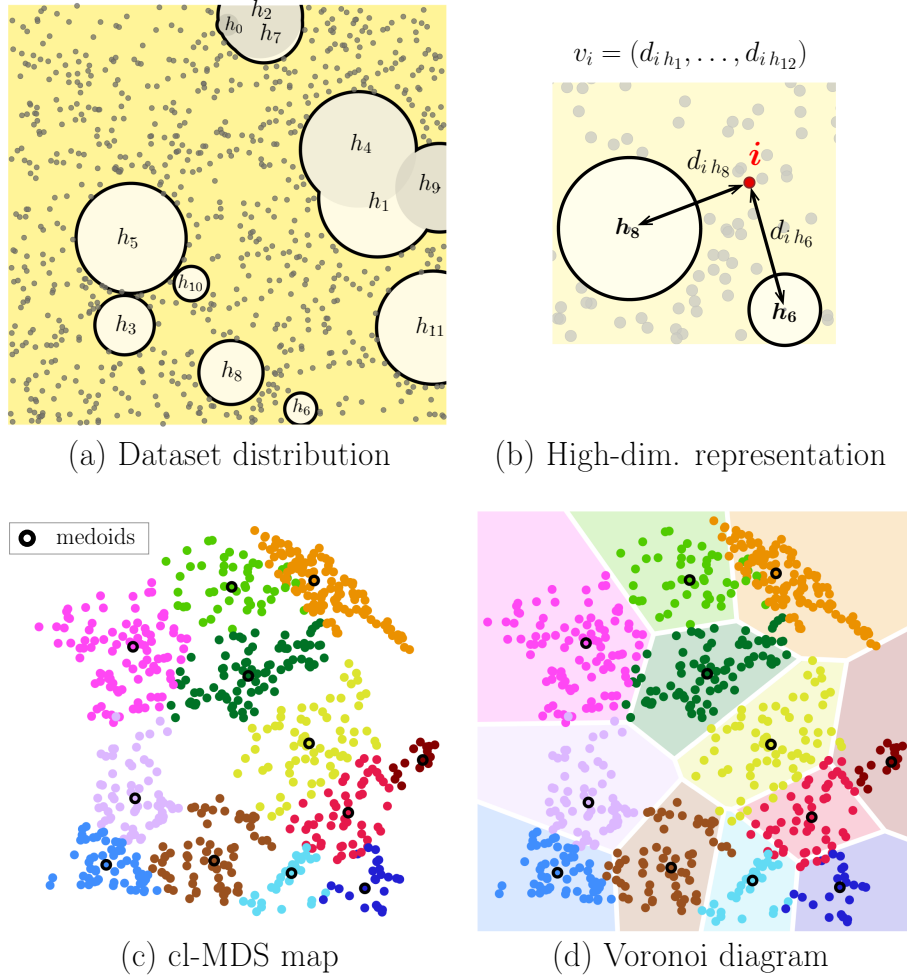


Figure 5: Simple example of cl-MDS applied to a high-dimensional dataset. The sample consists of 1000 points distributed in \mathbb{R}^2 as shown on panel (a), where $N_h = 12$. Their high-dimensional representation is obtained from the pairwise distances to each hole, illustrated on panel (b). Panels (c) and (d) show the cl-MDS embedding and the Voronoi diagram of the medoids, respectively.

Now that we have built some intuition regarding the advantages, disadvantages and hyperparameters of cl-MDS, we can apply it to more complex datasets. Also, advanced features such as sparsification and the corresponding estimation of the complete 2-dimensional representation are used in the following examples.

4.2 CHO structural database

The CHO database is a subset of the original dataset from Ref. (Golze et al., 2022), corresponding to a wide variety of CHO-containing materials. It contains 675 computer-

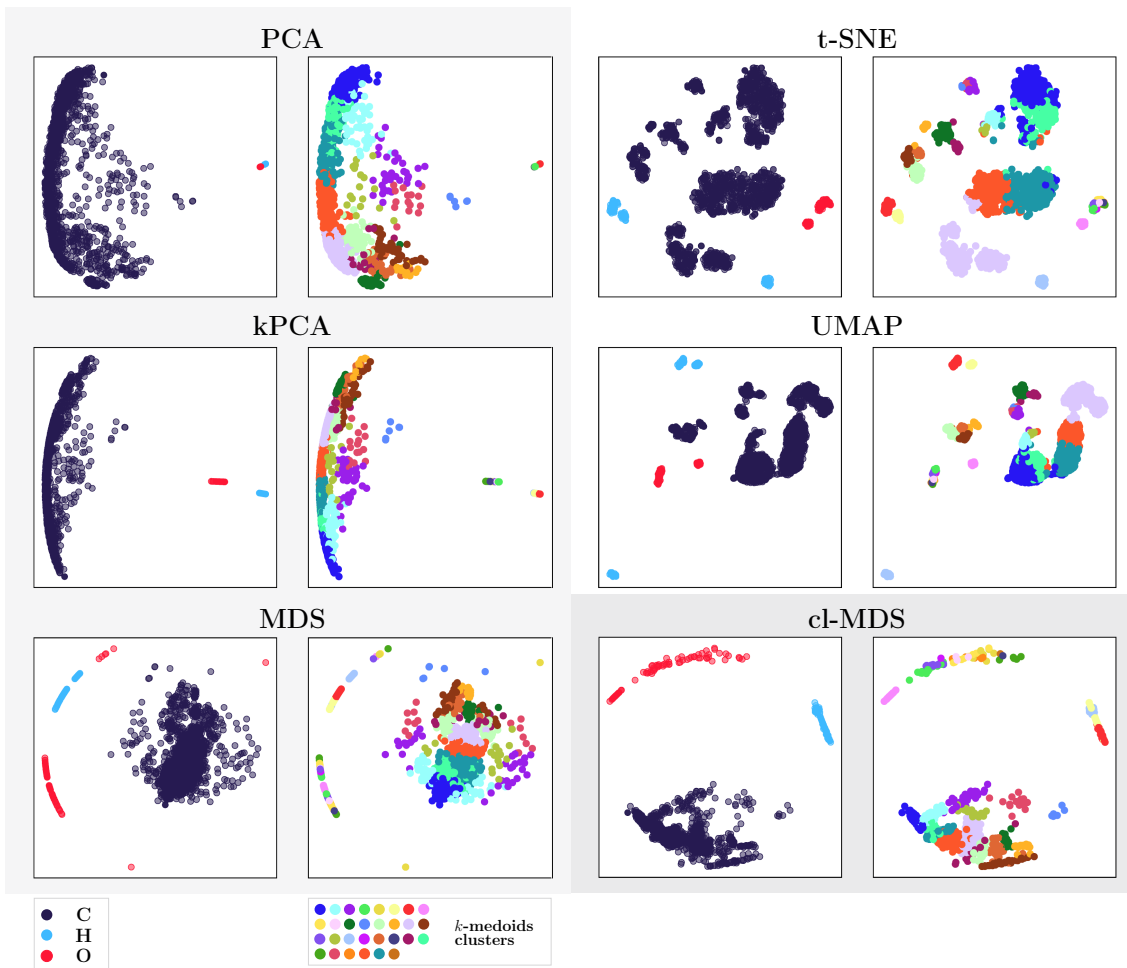


Figure 6: Embedding of 2000 random data points performed using several methods, where each point corresponds to an atom from the CHO database. Two plots are included per method/embedding: one color-coded according to chemical species (C, H, O) and another color-coded according to k -medoids clustering.

generated models of CHO materials, for a total of 151,556 unique atomic environments. Following the specifics described in Section 3, each data point corresponds to an atom represented by a SOAP descriptor of dimension $N_{\text{SOAP}} = 2700$, computed with the option "quippy_soap_turbo". This way, the dataset has an associated kernel distance based on the similarities between atomic environments defined within the chosen cutoff radii [see Eq. (19)]. Note the difference between using a cutoff sphere and restricting the number of neighbors as main criterion for defining the idea of environment. The former establishes how far the neighborhood of an atom stretches without assuming the number of nearest neighbors that populate that region. A cutoff sphere-based representation allows us to systematically compare atoms with differing numbers of neighbors.

We consider two approaches to dimensionality reduction: i) an overall embedding of a multispecies sample and ii) separated embeddings per chemical species (C, H, O). The former is shown on Fig. 6, with several dimensionality reduction techniques applied to a random sample of 2000 data points. Only those techniques that did not fail were included, illustrating the common visualizations available for an atomic sample. Here, the high-dimensional representation was computed using cutoff radii $r_{\text{soft}} = 3.75 \text{ \AA}$, $r_{\text{hard}} = 4.25 \text{ \AA}$. These radii ensured the convergence of the ML models trained in Ref. (Golze et al., 2022) and, therefore, retain enough relevant structural knowledge.

First, it is noteworthy that the most elementary chemical intuition is captured visually by PCA, kPCA and cl-MDS solely. A multispecies sample is characterized by higher dissimilarities among atoms from different chemical species, unless the central atom is explicitly neglected. That is, we would expect that a 2-dimensional representation of such sample reflects those dissimilarities with a proper separation of atomic species, particularly for metric-based methods. However, all MDS attempts failed to encode global H and O dissimilarities in terms of the pairwise distances in the embedded space, despite MDS being the quintessential method for pairwise distance preservation. On the other hand, manifold-based methods such as t-SNE and UMAP are misleading in this regard, since neither the distances nor the size of the clusters in their embeddings are meaningful. Even if they retain some global structures, Fig. 6 shows how relative positions between H clusters were lost.

Second, we incorporate cluster information from k -medoids into Fig. 6. Given that data clustering is independent of the embedding, we can compare how consistently each method preserves it. As expected, cl-MDS outperforms other methods since its algorithm is based on clustering preservation, overcoming the tendency of regular MDS to mix different clusters. Conversely, the usual "clustered-appearance" of t-SNE maps is not consistent with k -medoids clustering. Meanwhile, PCA, kPCA and UMAP tend to collapse smaller clusters irrespective of their relevance, obscuring their visualization. In particular, this issue happened with UMAP despite increasing its hyperparameter `min_dist`, which adjusts the minimum distance between embedded points.

Motivated by the clear separation between C, H and O atoms in Fig. 6, we computed the cl-MDS maps per chemical species, as shown in Fig. 7. In this second approach, each embedding includes all atoms from the same species within the CHO database, i.e., 135,618 C atoms, 7669 H atoms and 8269 O atoms. Sparsification support proved itself very handy, especially for carbon, combined with the estimation of the low-dimensional representation for the whole dataset (see Section 2.4). We found that a sparse set containing as few as 2 percent of the whole carbon dataset was representative enough when carefully selected, e.g., using a combination of random and CUR-based data points as well as precomputed medoids. Oxygen and hydrogen datasets, albeit smaller in size, also benefited from sparsification due to its improvement of MDS performance within cl-MDS computations.

Additionally, Fig. 7 contains two separate embeddings for each chemical species, computed from SOAP representations of the database with different cutoff radii: the radii already used in Fig. 6, and a shorter version with $r_{\text{soft}} = 1.75 \text{ \AA}$, $r_{\text{hard}} = 2.25 \text{ \AA}$. These visualizations illustrate the importance of the distance measure when performing dimensionality reduction. While using large radii retains more structural information, it also increases the complexity of the atomic environments and their overall dissimilarities. While the SOAP representation does not change its original dimensionality, which depends exclusively on the

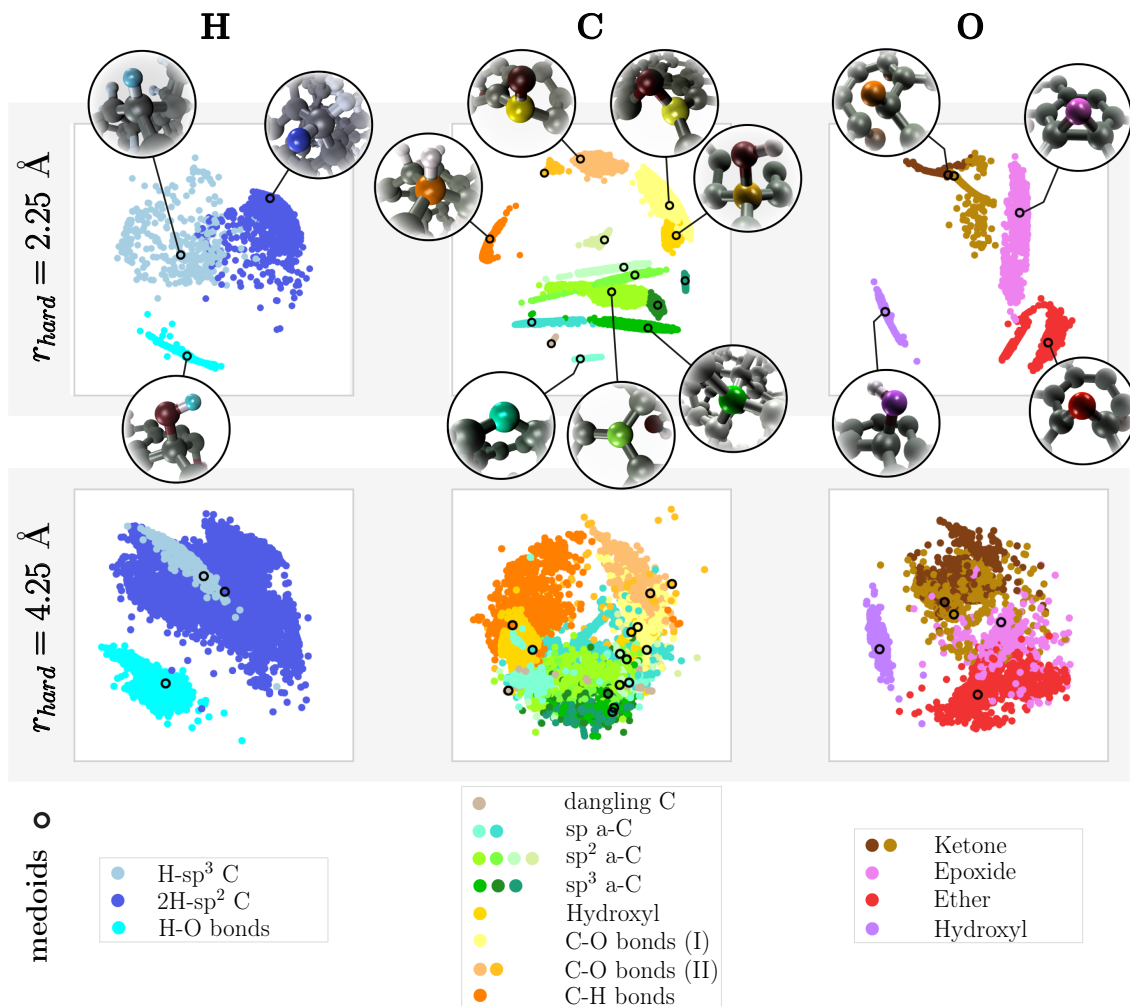


Figure 7: Visualization of the entire CHO database using cl-MDS. The embeddings were computed individually per chemical species (columns), considering high-dimensional representations with two different cutoff radii (rows). The medoids and clusters for the shortest radii ($r_{\text{soft}} = 1.75 \text{ \AA}$, $r_{\text{hard}} = 2.25 \text{ \AA}$) are highlighted in all embeddings, with their atomic motifs and their corresponding chemical denomination included.

number of basis functions used, the region of SOAP space spanned by the sample increases, effectively becoming more sparsely populated with increased averaged distances between data points, hindering data clustering. On the other hand, a small cutoff radius emphasizes first and second neighbors in the representation, allowing an straightforward connection between the embeddings and classical chemical motifs or functional groups in this example. That said, note that the same radii could be too small for molecular datasets for instance

(see Section 4.3); in practice, the choice of radii depends heavily on the dataset and the purpose of the visualization.

Since carbon has the richest structural landscape in this database, we eased the clustering and embedding process for carbon by applying cluster hierarchy, with $h = [15, 7, 3, 1]$ (see Section 2.4). We used a simpler clustering for hydrogen and oxygen, with $N_{\text{cl}} = 3$ and $N_{\text{cl}} = 5$, respectively. Besides the usual advantages of k -medoids versus k -means (Arora et al., 2016) (e.g., allowing for different sizes of clusters, being less sensitive to outliers), the knowledge of the medoids is itself valuable for visualization purposes. That is, we do not only obtain a 2-dimensional plot of the dataset, but also a representative per cluster that we can track back to the sample, as Fig. 7 illustrates. We have added labels that identify the clusters/medoids with classical chemical configurations (i.e., simple hybridizations and functional groups) to simplify the visualization, associating several clusters with the same label. However, the clustering was thorough enough to further distinguish between groups in terms of other structural features, such as angles or bond distances.

4.3 QM9 database

The QM9 database (Ramakrishnan et al., 2014) is a subset of a much larger database (the GDB-17 database (Ruddigkeit et al., 2012), with 166 billion molecules) carefully selected for a detailed sampling of the chemical space of small organic compounds. In particular, it contains 133,885 neutral organic molecules composed of carbon, hydrogen, oxygen, nitrogen and fluorine, up to nine "heavy" atoms (C, O, N, F). To represent QM9 we use SOAP vectors of dimension $N_{\text{SOAP}} = 7380$, obtained with the option "quippy_soap_turbo" and cutoff radii $r_{\text{soft}} = 3 \text{ \AA}$, $r_{\text{hard}} = 3.5 \text{ \AA}$ (similarly accurate SOAP vectors with lower dimensionality are available via SOAP compression with "quippy_soap_turbo_compress"). As discussed in Section 4.2, the difference between chemical species outweighs any other dissimilarity in a combined embedding; consequently, we performed a separate cl-MDS embedding per chemical species. A sparse set of 1000-2000 atoms depending on the species was used, carefully selected by combining k -medoids, random picking and a consistent clustering. The visualization of each atomic species was obtained through the estimation of the low-dimensional coordinates (see Section 2.4).

Figure 8 shows the resulting cl-MDS embeddings, which help us visualize the composition of the QM9 database. Here we can appreciate once again how cl-MDS performs worse when separating clusters for chemical species with richer variety of atomic environments, e.g., carbon. As opposed to the CHO example in Section 4.2 (see Fig. 7), C atoms were embedded with a simple hierarchy, $h = [15, 1]$, reducing the capability of cl-MDS to effectively differentiate additional nuances. Its combination with medoids information nonetheless highlights those subtleties via the corresponding molecular motifs, proving again the value of cluster information. Here, all the medoids were included, revealing the existence of other relevant properties, apart from the chemical species, such as the geometrical arrangement of the molecules. For instance, this is suggested by the absence of fluorine-related clusters in H, N and O embeddings despite its presence in several structures. Independently of the number of clusters, fluorine is not representative enough to weigh in the dissimilarities unless it is a first-nearest neighbor, i.e., with carbon.

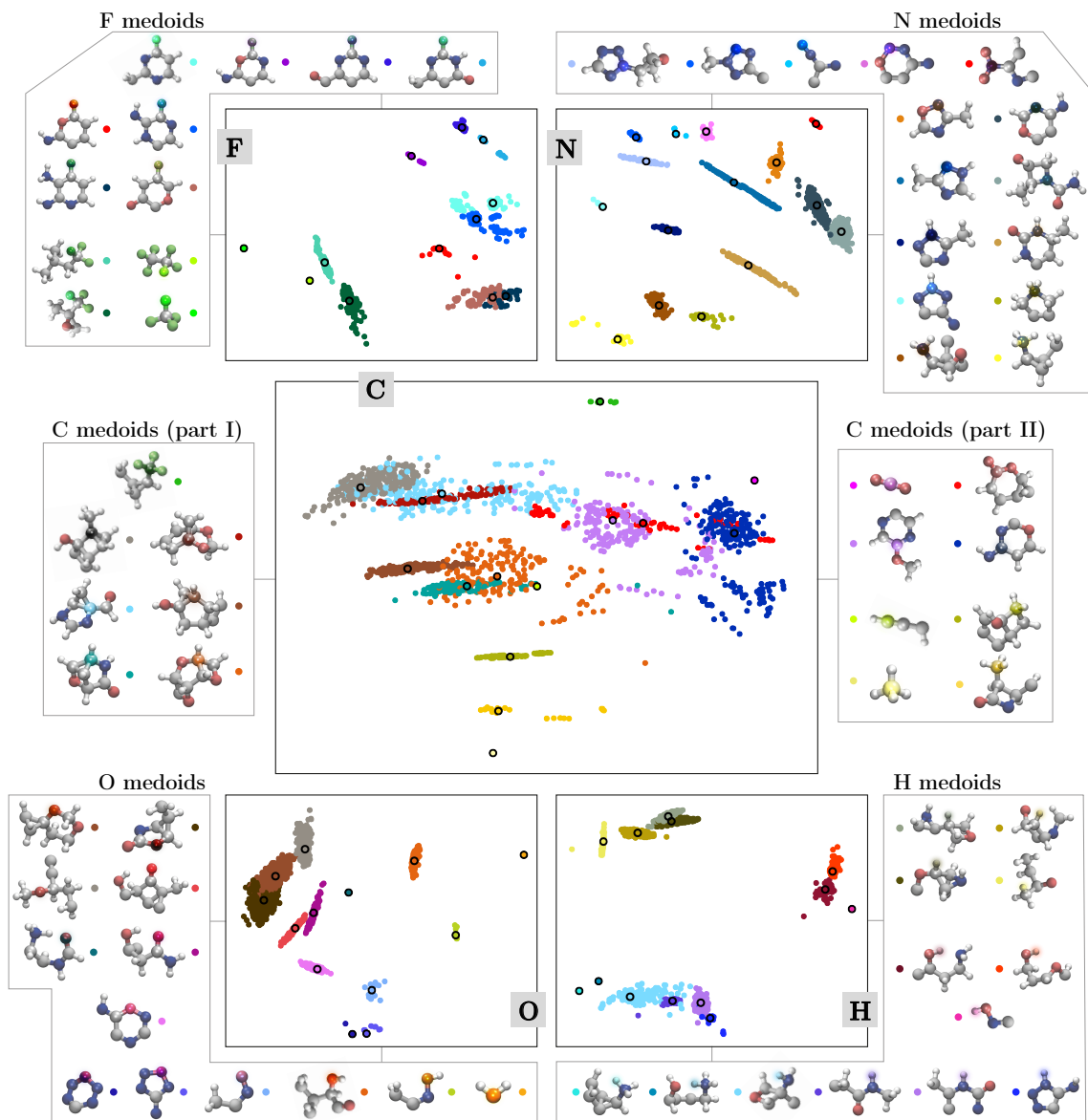


Figure 8: Visualization of the QM9 database through five cl-MDS mappings, one per atomic species (C, H, O, N, F). We show all the medoids and their atomic environments to illustrate the distribution of chemical and structural properties in each embedding, highlighting them in each molecular motif with the following colors: gray (C), white (H), red (O), blue (N) and green (F).

5. Conclusions and outlook

We have introduced a novel technique for data visualization called cluster MDS, which aims to capture high-dimensional local and global features adequately in a single 2-dimensional

representation. This issue is inadequately addressed by older methods due to limitations of their dimensionality reduction algorithms. More recent techniques still experience important limitations in this regard, such as the need for a “balancing” parameter that may crucially impact the structures preserved (e.g., UMAP, GLSPP (Cai, 2017)), or the imposition of specific metrics that limit their application to other fields (e.g., PHATE, DGL (Song et al., 2017)).

The cl-MDS algorithm is based on a combination of data clustering and data embedding through k -medoids and metric MDS, respectively, with any distance matrix (or dissimilarity measure) as accepted input. We have illustrated the effect of its main hyperparameter, the number of clusters, which can capture the local nuances in the visualization without affecting the overall structure preservation, once a minimum value is reached. This value depends on the dataset and impacts the quality of cl-MDS mappings, rendering our heuristic selection in this paper unsatisfactory. We will explore available criteria to automate this choice and increase its reliability. In its more advanced form, this hyperparameter accepts a hierarchy of clusters that eases the embedding of highly complex data and aids the visualization of big amounts of unlabelled data.

Additionally, cl-MDS can estimate the 2-dimensional coordinates of other points once a first embedding has been obtained. Given that our method partially inherits the decreasing performance of MDS with dataset size, this estimation is extremely useful when combined with the included sparsification support. However, its quality strongly depends on the chosen sparse set and needs to be carefully assessed. We will update the options for automated sparse selection available in the code as most robust alternatives arise. Other future improvements of the code include the optimization of its computational speed and memory requirements.

Its comparison with well-known methods such as PCA, kPCA, t-SNE, MDS and UMAP showed that cl-MDS improved visualization of different layers of locality, most notably compared to MDS performance. We applied it to datasets of sizes 10^3 to 10^6 and dimensionality up to 7380. In particular, we focused on atomic-structure examples to showcase all the functionality and advantages of this embedding tool, which includes specific recipes for atomic databases. Despite the value of manifold unfolding in other contexts, metric preservation is arguably the best approach for atomic databases. The comparison of atomic structures, as well as the study of their properties, usually involves some sort of similarity measure; therefore, its retention is invaluable in any visualization. Beyond the application to atomic structure datasets highlighted in this paper, we remark that cl-MDS is a general tool. Any dataset with relevant local and global structures can benefit from its use, whenever the data accepts the definition of a meaningful metric.

Acknowledgments and Disclosure of Funding

The authors are grateful for financial support from the Academy of Finland under projects #321713, #329483, #330488 and #347252, as well as computational resources provided by CSC – IT Center for Science and Aalto University’s Science-IT Project.

References

- P. Arora, D. Deepali, and S. Varshney. Analysis of k-means and k-medoids algorithm for big data. *Procedia Computer Science*, 78:507–512, 2016.
- S. R. Bahn and K. W. Jacobsen. An object-oriented scripting interface to a legacy electronic structure code. *Comput. Sci. Eng.*, 4(3):56–66, 2002.
- C. B. Barber, D. P. Dobkin, and H. T. Huhdanpaa. The quickhull algorithm for convex hulls. *ACM Trans. on Mathematical Software*, 22(4):469–483, 1996.
- A. P. Bartók, R. Kondor, and G. Csányi. On representing chemical environments. *Phys. Rev. B*, 87:184115, 2013.
- C. Bauckhage. Numpy / scipy recipes for data science: k-medoids clustering. University of Bonn, Germany, 2015.
- M. Belkin and P. Niyogi. Laplacian eigenmaps for dimensionality reduction and data representation. *Neural Comput.*, 15(6):1373–1396, 2003.
- E. Bertini, A. Tatu, and D. Keim. Quality metrics in high-dimensional data visualization: an overview and systematization. *IEEE Trans Vis Comput Graph.*, 17(12):2203–2212, 2011.
- I. Borg and P. J. F. Groenen. *Modern Multidimensional Scaling*. Springer, New York, NY, 2005.
- W. Cai. A dimension reduction algorithm preserving both global and local clustering structure. *Knowledge-Based Systems*, 118:191–203, 2017.
- M. A. Caro. Optimizing many-body atomic descriptors for enhanced computational performance of machine learning based interatomic potentials. *Phys. Rev. B*, 100:024112, 2019.
- M. A. Caro. *soap_turbo* library, https://github.com/libAtoms/soap_turbo, accessed September 14, 2022.
- M. A. Caro and P. Hernández-León. *cl-MDS* repository, <https://github.com/mcaroba/cl-MDS>, accessed September 14, 2022a.
- M. A. Caro and P. Hernández-León. *fast-kmedoids*, <https://github.com/mcaroba/fast-kmedoids>, accessed September 14, 2022b.
- M. A. Caro, A. Aarva, V. L. Deringer, G. Csányi, and T. Laurila. Reactivity of amorphous carbon surfaces: rationalizing the role of structural motifs in functionalization using machine learning. *Chem. Mater.*, 30:7446, 2018.
- M. Ceriotti, G. A. Tribello, and M. Parrinello. Simplifying the representation of complex free-energy landscapes using sketch-map. *Proceedings of the National Academy of Sciences*, 108(32):13023–13028, 2011.

- L. Chen and A. Buja. Local multidimensional scaling for nonlinear dimension reduction, graph drawing, and proximity analysis. *Journal of the American Statistical Association*, 104(485):209–219, 2009.
- B. Cheng, R.-R. Griffiths, S. Wengert, C. Kunkel, T. Stenczel, B. Zhu, V. L. Deringer, N. Bernstein, J. T. Margraf, K. Reuter, and G. Csányi. Mapping materials and molecules. *Accounts Chem. Res.*, 53(9):1981–1991, 2020.
- R. R. Coifman and S. Lafon. Diffusion maps. *Applied and Computational Harmonic Analysis*, 21(1):5–30, 2006. Special Issue: Diffusion Maps and Wavelets.
- R. R. Coifman, S. Lafon, A. B. Lee, M. Maggioni, B. Nadler, F. Warner, and S. W. Zucker. Geometric diffusions as a tool for harmonic analysis and structure definition of data: Multiscale methods. *Proceedings of the National Academy of Sciences*, 102(21):7432–7437, 2005.
- G. Csányi, S. Winfield, J. Kermode, M. C. Payne, A. Comisso, A. De Vita, and N. Bernstein. Expressive programming for computational physics in fortran 95+. *IoP Comput. Phys. Newsletter*, page Spring 2007, 2007.
- S. De and M. Ceriotti. Interactive sketchmap visualizer, 2019. URL <https://doi.org/10.5281/zenodo.3541831>.
- S. De, A. P. Bartók, G. Csányi, and M. Ceriotti. Comparing molecules and solids across structural and alchemical space. *Phys. Chem. Chem. Phys.*, 18:13754, 2016.
- D. L. Donoho and C. Grimes. Hessian eigenmaps: Locally linear embedding techniques for high-dimensional data. *Proceedings of the National Academy of Sciences*, 100(10):5591–5596, 2003.
- P. Drineas, R. Kannan, and M. W. Mahoney. Fast monte-carlo algorithms for matrices iii: Computing a compressed approximate matrix decomposition. *SIAM Journal on Computing*, 36(1):184–206, 2006.
- D. H. Eberly. Perspective mappings, Accessed September 14, 2022. <https://www.geometrictools.com/Documentation/PerspectiveMappings.pdf>.
- G. Fraux, R. Cersonsky, and M. Ceriotti. Chemiscope: interactive structure-property explorer for materials and molecules. *Journal of Open Source Software*, 5:2117, 2020.
- D. Golze, M. Hirvensalo, P. Hernández-León, A. Aarva, J. Etula, T. Susi, P. Rinke, T. Laurila, and M. A. Caro. Accurate computational prediction of core-electron binding energies in carbon-based materials: A machine-learning model combining density-functional theory and gw. *Chemistry of Materials*, 34(14):6240–6254, 2022.
- P. Gritzmann and V. Klee. On the complexity of some basic problems in computational convexity: I. containment problems. *Discrete Mathematics*, 136(1):129–174, 1994.
- M. Halkidi, Y. Batistakis, and M. Vazirgiannis. On clustering validation techniques. *Journal of Intelligent Information Systems*, 17, 2001.

- C. R. Harris, K. J. Millman, S. J. van der Walt, R. Gommers, P. Virtanen, D. Cournapeau, E. Wieser, J. Taylor, S. Berg, N. J. Smith, R. Kern, M. Picus, S. Hoyer, M. H. van Kerkwijk, M. Brett, A. Haldane, J. Fernández del Río, M. Wiebe, P. Peterson, P. Gérard-Marchant, K. Sheppard, T. Reddy, W. Weckesser, H. Abbasi, C. Gohlke, and T. E. Oliphant. Array programming with NumPy. *Nature*, 585(7825):357–362, 2020.
- J. A. Hartigan and M. A. Wong. Algorithm as 136: A k-means clustering algorithm. *Journal of the Royal Statistical Society. Series C (Applied Statistics)*, 28(1):100–108, 1979.
- T. Hastie, R. Tibshirani, and J. Friedman. *The Elements of Statistical Learning*. Springer, 2009.
- L. Himanen, M. O. J. Jäger, E. V. Morooka, F. Federici Canova, Y. S. Ranawat, D. Z. Gao, P. Rinke, and A. S. Foster. D`Scribe`: Library of descriptors for machine learning in materials science. *Computer Physics Communications*, 247:106949, 2020.
- H. Hotelling. Analysis of a complex of statistical variables into principal components. *Journal of Educational Psychology*, 24(6):417–441, 1933.
- L. Kaufman and P. Rousseeuw. Clustering by means of medoids. In *Statistical Data Analysis Based on the L1 Norm and Related Methods*. Ed. Elsevier, 1987.
- L. Kaufman and P. J. Rousseeuw. *Finding Groups in Data: An Introduction to Cluster Analysis*. New York John Wiley & Sons, 1990.
- J. R. Kermode. f90wrap: an automated tool for constructing deep python interfaces to modern fortran codes. *J. Phys. Condens. Matter*, 2020.
- J. B. Kruskal. Multidimensional scaling by optimizing goodness of fit to a nonmetric hypothesis. *Psychometrika*, 29:1–27, 1964a.
- J. B. Kruskal. Nonmetric multidimensional scaling: A numerical method. *Psychometrika*, 29:115–129, 1964b.
- A. H. Larsen, J. J. Mortensen, J. Blomqvist, I. E. Castelli, R. Christensen, M. Dulak, J. Friis, M. N. Groves, B. Hammer, C. Hargus, E. D. Hermes, P. C. Jennings, P. B. Jensen, J. Kermode, J. R. Kitchin, E. L. Kolsbjerg, J. Kubal, K. Kaasbjerg, S. Lysgaard, J. B. Maronsson, T. Maxson, T. Olsen, L. Pastewka, A. Peterson, C. Rostgaard, J. Schiøtz, O. Schütt, M. Strange, K. S. Thygesen, T. Vegge, L. Vilhelmsen, M. Walter, Z. Zeng, and K. W. Jacobsen. The Atomic Simulation Environment – A Python library for working with atoms. *J. Phys.: Condens. Matter*, 29:273002, 2017.
- J. Leskovec, A. Rajaraman, and J. D. Ullman. *Mining of Massive Datasets*. Cambridge University Press, 2020.
- Y. Liu, Z. Li, H. Xiong, X. Gao, and J. Wu. Understanding of internal clustering validation measures. *2010 IEEE International Conference on Data Mining*, pages 911–916, 2010.
- K. Lui, G. W. Ding, R. Huang, and R. McCann. Dimensionality reduction has quantifiable imperfections: Two geometric bounds. *Advances in Neural Information Processing Systems*, 31:8453–8463, 2018.

- J. Macqueen. Some methods for classification and analysis of multivariate observations. *Proceedings of the 5th Berkeley Symposium on Mathematical Statistics and Probability*, 1:281–297, 1967.
- M. W. Mahoney and P. Drineas. Cur matrix decompositions for improved data analysis. *Proceedings of the National Academy of Sciences*, 106(3):697–702, 2009.
- M. W. Mahoney, M. Maggioni, and P. Drineas. Tensor-cur decompositions for tensor-based data. *SIAM Journal on Matrix Analysis and Applications*, 30(3):957–987, 2008.
- L. McInnes, J. Healy, and J. Melville. Umap: Uniform manifold approximation and projection for dimension reduction, 2020.
- K. R. Moon, D. van Dijk, Z. Wang, S. Gigante, D. B. Burkhardt, W. S. Chen, K. Yim, A. van den Elzen, M. J. Hirn, R. R. Coifman, N. B. Ivanova, G. Wolf, and S. Krishnaswamy. Visualizing structure and transitions in high-dimensional biological data. *Nat Biotechnol*, 37:1482–1492, 2019.
- A. Y. Ng, M. I. Jordan, and Y. Weiss. On spectral clustering: Analysis and an algorithm. In *Advances in Neural Information Processing Systems*, pages 849–856. MIT Press, 2001.
- F. Pedregosa, G. Varoquaux, A. Gramfort, V. Michel, B. Thirion, O. Grisel, M. Blondel, P. Prettenhofer, R. Weiss, V. Dubourg, J. Vanderplas, A. Passos, D. Cournapeau, M. Brucher, M. Perrot, and E. Duchesnay. Scikit-learn: Machine learning in Python. *Journal of Machine Learning Research*, 12:2825–2830, 2011.
- P. Peterson. F2PY: a tool for connecting Fortran and Python programs. *Int. J. Comput. Sci. Eng.*, 4:296, 2009.
- R. Ramakrishnan, P. O. Dral, M. Rupp, and O. A. von Lilienfeld. Quantum chemistry structures and properties of 134 kilo molecules. *Scientific Data*, 1, 2014.
- J. Richter-Gebert. *Perspectives on Projective Geometry: A Guided Tour Through Real and Complex Geometry*. Springer, 2010.
- S. T. Roweis and L. K. Saul. Nonlinear dimensionality reduction by locally linear embedding. *Science*, 290(5500):2323–2326, 2000.
- L. Ruddigkeit, R. van Deursen, L. C. Blum, and J. L. Reymond. Enumeration of 166 billion organic small molecules in the chemical universe database gdb-17. *J. Chem. Inf. Model.*, 52:2864–2875, 2012.
- P. J. Schneider and D. H. Eberly. *Geometric Tools for Computer Graphics*. Morgan Kaufmann publishers, Elsevier Science, 2003.
- B. Schölkopf. The kernel trick for distances. In *Advances in Neural Information Processing Systems*, volume 13. MIT Press, 2000.
- B. Schölkopf, A. Smola, and K.-R. Müller. Nonlinear Component Analysis as a Kernel Eigenvalue Problem. *Neural Computation*, 10(5):1299–1319, 1998.

- D. M. Y. Sommerville. *An Introduction to the Geometry of N Dimensions*. Methuen & Co., London, 1929.
- Y. Song, J. Wang, L. Qi, W. Yuan, Zhensu, M. Yu, and J. Qu. A new algorithm for preserving global and local structures in supervised dimensionality reduction. *7th IEEE International Conference on Electronics Information and Emergency Communication (ICEIEC)*, pages 244–247, 2017.
- J. Tenenbaum, V. Silva, and J. Langford. A global geometric framework for nonlinear dimensionality reduction. *Science*, 290:2319–2323, 2000.
- F. S. Tsai. A visualization metric for dimensionality reduction. *Expert Systems with Applications*, 39(2):1747–1752, 2012.
- L. van der Maaten. Accelerating t-sne using tree-based algorithms. *Journal of Machine Learning Research*, 15(93):3221–3245, 2014.
- L. van der Maaten and G. Hinton. Visualizing data using t-sne. *Journal of Machine Learning Research*, 9(86):2579–2605, 2008.
- J. Vanderplas. *Comparison of Manifold Learning methods*, accessed September 14, 2022. URL https://scikit-learn.org/stable/auto_examples/manifold/plot_compare_methods.html.
- J. Venna and S. Kaski. Local multidimensional scaling. *Neural Networks*, 19(6):889–899, 2006.
- P. Virtanen, R. Gommers, T. E. Oliphant, M. Haberland, T. Reddy, D. Cournapeau, E. Burovski, P. Peterson, W. Weckesser, J. Bright, S. J. van der Walt, M. Brett, J. Wilson, K. J. Millman, N. Mayorov, A. R. J. Nelson, E. Jones, R. Kern, E. Larson, C. J. Carey, Í. Polat, Y. Feng, E. W. Moore, J. VanderPlas, D. Laxalde, J. Perktold, R. Cimrman, I. Henriksen, E. A. Quintero, C. R. Harris, A. M. Archibald, A. H. Ribeiro, F. Pedregosa, P. van Mulbregt, A. Vijaykumar, A. P. Bardelli, A. Rothberg, A. Hilboll, A. Kloeckner, A. Scopatz, A. Lee, A. Rokem, C. N. Woods, C. Fulton, C. Masson, C. Häggström, C. Fitzgerald, D. A. Nicholson, D. R. Hagen, D. V. Pasechnik, E. Olivetti, E. Martin, E. Wieser, F. Silva, F. Lenders, F. Wilhelm, G. Young, G. A. Price, G.-L. Ingold, G. E. Allen, G. R. Lee, H. Audren, I. Probst, J. P. Dietrich, J. Silterra, J. T. Webber, J. Slavič, J. Nothman, J. Buchner, J. Kulick, J. L. Schönberger, J. V. de Miranda Cardoso, J. Reimer, J. Harrington, J. L. C. Rodríguez, J. Nunez-Iglesias, J. Kuczynski, K. Tritz, M. Thoma, M. Newville, M. Kümmerer, M. Bolingbroke, M. Tartre, M. Pak, N. J. Smith, N. Nowaczyk, N. Shebanov, O. Pavlyk, P. A. Brodtkorb, P. Lee, R. T. McGibbon, R. Feldbauer, S. Lewis, S. Tygier, S. Sievert, S. Vigna, S. Peterson, S. More, T. Pudlik, T. Oshima, T. J. Pingel, T. P. Robitaille, T. Spura, T. R. Jones, T. Cera, T. Leslie, T. Zito, T. Krauss, U. Upadhyay, Y. O. Halchenko, Y. Vázquez-Baeza, and SciPy 1.0 Contributors. SciPy 1.0: Fundamental Algorithms for Scientific Computing in Python. *Nature Methods*, 17:261–272, 2020.
- M. J. Willartt, F. Musli, and M. Ceriotti. Atom-density representations for machine learning. *The Journal of Chemical Physics*, 150(15):154110, 2019.

- Z. Zhang and J. Wang. Mlle: Modified locally linear embedding using multiple weights. In *Advances in Neural Information Processing Systems*, volume 19, pages 1593–1600. MIT Press, 2007.
- Z. Zhang and H. Zha. Principal manifolds and nonlinear dimension reduction via local tangent space alignment. *arXiv*, 2002.